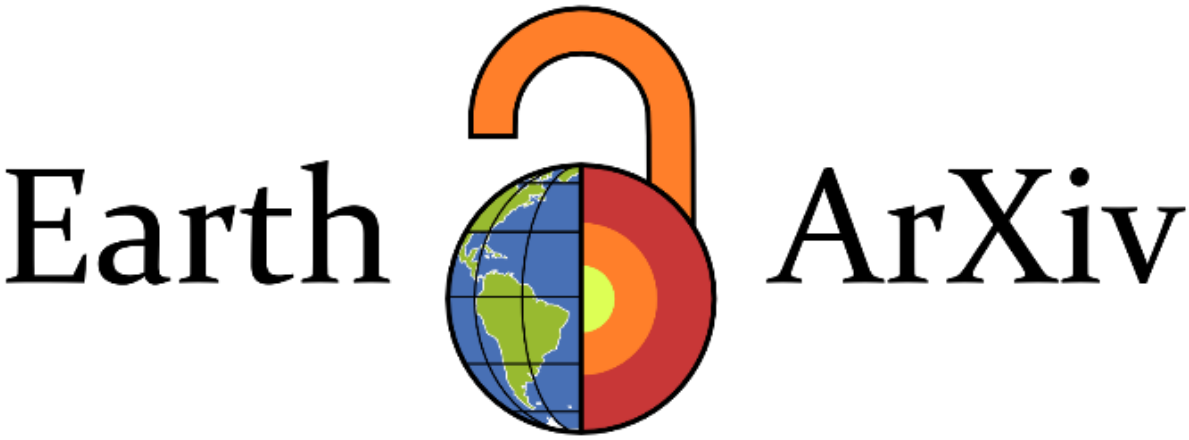

Topographies, and Geoid/Gravity Anomalies from Global Mantle Flow Models

Project Representative
Masaki Yoshida Research Institute for Marine Geodynamics, Japan Agency for Marine-Earth Science and Technology

Authors
Masaki Yoshida*[1]
*[1] Research Institute for Marine Geodynamics, Japan Agency for Marine-Earth Science and Technology

Keywords: mantle flow, topography, core–mantle boundary, geoid anomaly, gravity anomaly

1. Introduction

The ultimate goal of this project is to understand the thermal, compositional, and rheological structures of the present-day Earth's mantle under the constraints imposed by surface observations, such as plate motion, top surface and core–mantle boundary (CMB) topographies, and geoid and gravity anomalies. With a limited model that ignores the mantle lateral viscosity variations and truncates the short-wavelength structure, the surface observations obtained from a computed instantaneous global mantle flow model can be compared with those obtained from a semianalytical method using a propagator matrix [1]. In this study, the formulations of the surface observations and the evaluation of the misfits of the results obtained from semianalytical and numerical methods are presented.

2. Spherical harmonic expansions of geoid and gravity anomalies

The gravitational potential V is related to the density ρ through the following Poisson equation:

$$\nabla^2 V = -4\pi G\rho, \tag{1}$$

where G is the universal gravitational constant. The potential anomaly δV from a density anomaly δ also satisfies the Poisson equation:

$$\nabla^2 \delta V = -4\pi G\delta\rho. \tag{2}$$

The geoid anomaly δN at the Earth's top surface (i.e., radius $r = r_1$) is obtained by dividing δV by the radial derivative of the potential anomaly, which corresponds to the gravitational acceleration at the top surface $g(r_1)$:

$$\delta N(r_1) \equiv \frac{\delta V(r_1)}{-\partial V(r)/\partial r\big|_{r=r_1}} = \frac{\delta V(r_1)}{g(r_1)}. \tag{3}$$

The potential and density anomalies are expressed in terms of an infinite series of radius functions multiplied by spherical harmonic functions, Y^{lmi}, at each surface along the latitude and longitude of θ and φ, respectively, where l is the degree, m is the order, and i is the sine or cosine terms.

$$\begin{aligned}\delta V(r,\theta,\phi) &= \delta V^{lmi}(r,\theta,\phi)Y^{lmi}(\theta,\phi),\\ \delta\rho(r,\theta,\phi) &= \delta\rho^{lmi}(r,\theta,\phi)Y^{lmi}(\theta,\phi),\end{aligned} \tag{4}$$

The solution is solved by considering the density perturbation of the thickness dr at a specified radius $r = b$. The inner and outer solutions for the potential anomaly at $r = b$ satisfy:

$$\delta V^{lmi}(r) = \begin{cases} \dfrac{4\pi G}{2l+1} b\delta\rho^{lmi}(b)dr\left(\dfrac{r}{b}\right)^{l} & \text{if } r < b \\ \dfrac{4\pi G}{2l+1} b\delta\rho^{lmi}(b)dr\left(\dfrac{b}{r}\right)^{l+1} & \text{if } r \geq b \end{cases}. \tag{5}$$

For the Earth's interior with a radius of $r = r_1$, the anomalous potential at the top surface is given by

$$\delta V^{lmi}(r_1) = \frac{4\pi G}{2l+1} r\delta\rho^{lmi}(r)dr\left(\frac{r}{r_1}\right)^{l+1}. \tag{6}$$

Therefore, the geoid and gravity anomalies at the top surface are given as:

$$\begin{aligned}&\delta N^{lmi}(r_1)\\ &= \frac{\delta V^{lmi}(r_1)}{g(r_1)} = \frac{4\pi G}{(2l+1)g(r_1)} r\delta\rho^{lmi}(r)dr\left(\frac{r}{r_1}\right)^{l+1},\end{aligned} \tag{7}$$

$$\begin{aligned}\delta g^{lmi}(r_1) &= -\frac{\partial\delta V^{lmi}(r_1)}{\partial r}\\ &= -\frac{4\pi G(l+2)}{2l+1}\delta\rho^{lmi}(r)dr\left(\frac{r}{r_1}\right)^{l+1}\\ &= -\frac{(l+2)g(r_1)}{r}\delta N^{lmi}(r).\end{aligned} \tag{8}$$

For the Earth's mantle, with outer and inner radii of r_1 and r_0, respectively, the total geoid anomaly is the internal density anomaly integrated from r_0 to r_1 and the density anomaly due to the topographic deflection at the top surface and CMB. Thus, the net geoid and gravity anomalies derived from all three

contributions are expressed as follows:

$$\delta N^{lmi}(r_1) = \frac{4\pi G}{(2l+1)g(r_1)}\left[\int_{r_0}^{r_1} r\delta\rho^{lmi}(r)dr\left(\frac{r}{r_1}\right)^{l+1} + r_1\Delta\rho_1\delta r_1^{lmi} + r_0\Delta\rho_0\delta r_0^{lmi}\left(\frac{r_0}{r_1}\right)^{l+1}\right], \quad (9)$$

$$\delta g^{lmi}(r_1) = -\frac{4\pi G(l+2)}{2l+1}\left[\int_{r_0}^{r_1}\delta\rho^{lmi}(r)dr\left(\frac{r}{r_1}\right)^{l+1} + \Delta\rho_1\delta r_1^{lmi} + \Delta\rho_0\delta r_0^{lmi}\left(\frac{r_0}{r_1}\right)^{l+1}\right], \quad (10)$$

where $\Delta\rho_1$ and $\Delta\rho_0$ are the density differences at the top surface and CMB, respectively. The normal stresses acting on the top surface and CMB, σ_{rr} (positive for extension), are expressed as follows:

$$\delta\sigma_{rr}(r_1) = p(r_1) - 2\eta(r_1)\left.\frac{\partial v_r}{\partial r}\right|_{r=r_1},$$
$$\delta\sigma_{rr}(r_0) = -p(r_0) + 2\eta(r_0)\left.\frac{\partial v_r}{\partial r}\right|_{r=r_0}, \quad (11)$$

where p and η are the dynamic pressure and viscosity, respectively. The topographies at the top surface and CMB are given by

$$\delta r_1^{lmi} = \frac{\delta\sigma_{rr}^{lmi}(r_1)}{\Delta\rho_1 g(r_1)}, \quad \delta r_0^{lmi} = \frac{\delta\sigma_{rr}^{lmi}(r_0)}{\Delta\rho_0 g(r_0)}. \quad (12)$$

3. Calculations of geoid and gravity anomalies

The instantaneous mantle flow was calculated numerically and semianalytically using the mantle convection code ConvGS and the propagator matrix method, respectively. Following a previous study [2], the density anomaly in the mantle was converted from the S-wave velocity anomaly using seismic tomography and global slab models. The mantle viscosity is considered to be of three layers, i.e., the lithosphere at depths of 0–100 km, the upper mantle at depths of 100–660 km, and the lower mantle at depths of 660–2,891 km. The viscosity contrast between the lithosphere and upper mantle ($\Delta\eta_{lit}$) varied from 1 to 100, and that between the lower and upper mantles ($\Delta\eta_{lwm}$) varied from 1 to 100.

In the propagator matrix method, the modeled mantle thickness is divided into N discrete layers, and the density anomaly within each layer is assumed to be concentrated in the center of each discrete layer. In the calculation, N is fixed at 290, which is a sufficient resolution for the three-layer model. Thus, Eqs. 9 and 10 can be rewritten as follows:

$$\delta N^{lmi}(r_1) = \frac{4\pi G}{(2l+1)g(r_1)}\left[\sum_{n=1}^{N}\left\{\delta\rho_n^{lmi} r_n\left(\frac{r_n}{r_1}\right)^{l+1}(r_{n+1/2} - r_{n-1/2})\right\} + r_1\Delta\rho_1\delta r_1^{lmi} + r_0\Delta\rho_0\delta r_0^{lmi}\left(\frac{r_0}{r_1}\right)^{l+1}\right], \quad (13)$$

$$\delta g^{lmi}(r_1) = -\frac{4\pi G(l+2)}{2l+1}\left[\sum_{n=1}^{N}\left\{\delta\rho_n^{lmi}\left(\frac{r_n}{r_1}\right)^{l+1}(r_{n+1/2} - r_{n-1/2})\right\} + \Delta\rho_1\delta r_1^{lmi} + \Delta\rho_0\delta r_0^{lmi}\left(\frac{r_0}{r_1}\right)^{l+1}\right], \quad (14)$$

where r_n is the radius of the center of the n-th discrete layer, $r_{n\text{-}1/2}$ and $r_{n+1/2}$ are the radii of the bottom and top of the n-th discrete layer.

For the numerical model, the density anomaly is assumed to be uniformly distributed in the vertical direction within each computational grid. The number of grids in the radial direction is set to $N = 128$. Thus, Eqs. 9 and 10 can be rewritten as follows:

$$\delta N^{lmi}(r_1) = \frac{4\pi G}{(2l+1)g(r_1)}\left[\int_{r_{n-1/2}}^{r_{n+1/2}}\delta\rho_n^{lmi} r_n\left(\frac{r_n}{r_1}\right)^{l+1} dr + r_1\Delta\rho_1\delta r_1^{lmi} + r_0\Delta\rho_0\delta r_0^{lmi}\left(\frac{r_0}{r_1}\right)^{l+1}\right]$$
$$= \frac{4\pi G}{(2l+1)g(r_1)}\left[\frac{1}{r_1^{l+1}(l+3)}\sum_{n=1}^{N}\delta\rho_n^{lmi}(r_{n+1/2}^{l+3} - r_{n-1/2}^{l+3}) + r_1\Delta\rho_1\delta r_1^{lmi} + r_0\Delta\rho_0\delta r_0^{lmi}\left(\frac{r_0}{r_1}\right)^{l+1}\right], \quad (15)$$

$$\delta g^{lmi}(r_1) = -\frac{4\pi G(l+2)}{2l+1}\left[\int_{r_{n-1/2}}^{r_{n+1/2}}\delta\rho_n^{lmi}\left(\frac{r_n}{r_1}\right)^{l+1} dr + \Delta\rho_1\delta r_1^{lmi} + \Delta\rho_0\delta r_0^{lmi}\left(\frac{r_0}{r_1}\right)^{l+1}\right]$$
$$= -\frac{4\pi G(l+2)}{2l+1}\left[\frac{1}{r_1^{l+1}(l+2)}\sum_{n=1}^{N}\delta\rho_n^{lmi}(r_{n+1/2}^{l+2} - r_{n-1/2}^{l+2}) + \Delta\rho_1\delta r_1^{lmi} + \Delta\rho_0\delta r_0^{lmi}\left(\frac{r_0}{r_1}\right)^{l+1}\right]. \quad (16)$$

4. Results

Figure 1 shows the top surface and CMB topographies and the geoid and gravity anomalies for the model with $\Delta\eta_{lit} = 1$ and $\Delta\eta_{lwm} = 30$ from the semianalytical and numerical methods. In this model, a highly viscous lower mantle tended to reproduce the observed geoid pattern, namely the positive geoid anomaly in the western part of the Pacific, Africa to the North Atlantic, and the western margin of South America. The spatial patterns and magnitudes of the top surface and CMB topographies and the geoid and gravity anomalies obtained using the two methods were consistent.

The misfits of the geophysical patterns between the semianalytical and numerical methods for all models are shown in Figure 2. The results show that the misfits are almost below a few percent for all degrees. Although the misfits reach approximately 10% at the lowest degrees when $\Delta\eta_{lit}$ or $\Delta\eta_{lwm}$ is a large value, there seems to be no remarkable tendency of misfits at each degree among the models with different values of $\Delta\eta_{lit}$ and $\Delta\eta_{lwm}$. This result suggests that the misfits between the two methods depend on the spatial pattern of the mantle flow rather than on differences in the potential accuracy of the numerical solutions.

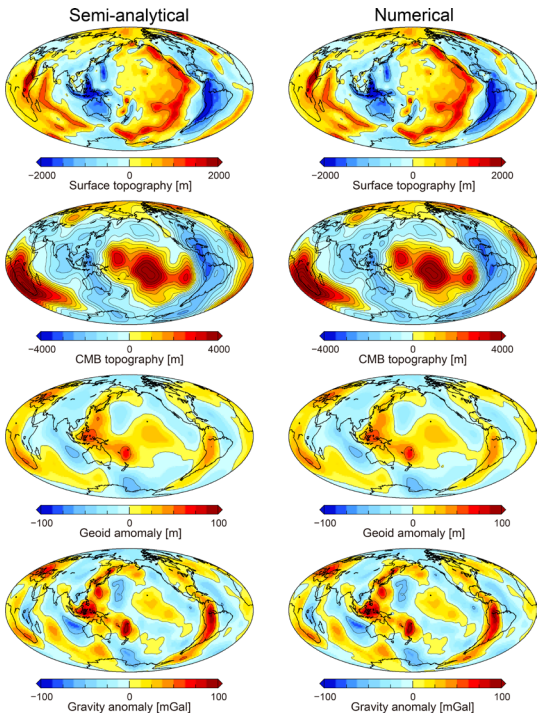

Fig. 1. Top surface and CMB topographies and geoid and gravity anomalies obtained from the semianalytical (left panels) and numerical (right panels) methods with $\Delta\eta_{lit} = 1$ and $\Delta\eta_{lwm} = 30$.

5. Concluding remarks

In this report, the misfits of topographies and geoid and gravity anomalies obtained from semianalytical and numerical calculations are evaluated. Because the pattern of mantle convection strongly depends on various model parameters [3], surface observations are useful for constraining the mantle structure. In the future, using a time-dependent mantle convection model, the relationship between temporal changes not only in these surface observations but also in the surface environment will be studied, e.g., long-term sea level changes that are indirectly related to solid-earth dynamics, including the supercontinent cycle and evolution of oceanic plates [4].

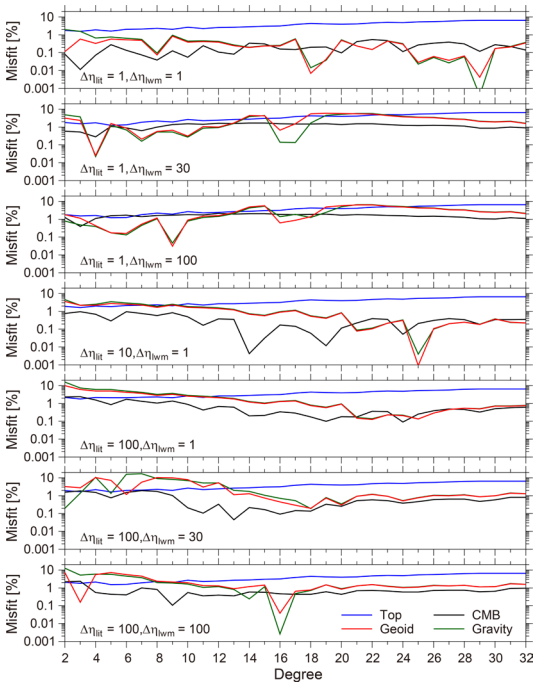

Fig. 2. Misfits of the top surface and CMB topographies (blue and black lines) and geoid and gravity anomalies (red and green lines) as a function of spherical harmonic degrees up to 32 for each model between the semianalytical and numerical methods. $\Delta\eta_{lit}$ and $\Delta\eta_{lwm}$ are the viscosity contrast of the lithosphere and lower mantle relative to the reference upper mantle, respectively.

References

[1] B.H. Hager and R.W. Clayton. "Constraints on the structure of mantle convection using seismic observations, flow models and the geoid," In: W.R. Peltier (Ed.), *Mantle Convection: Plate Tectonics and Global Dynamics*. Gordon and Breach, New York, pp. 657–763, 1989.

[2] M. Yoshida. "Stress state of the stable part of the Pacific plate predicted by a numerical model of global mantle flow coupled with plate motion," *Lithosphere*. vol. 2023, no. 1, pp. 6563534, 2023.

[3] M. Yoshida. "Stress regimes for the transition to stagnant-lid convection in the terrestrial mantle," *Planet. Space Sci.* vol. 238, pp. 105794, 2023.

[4] M. Yoshida. "Effect of the supercontinent cycle on the longest-term sea-level change from a simple conceptual and theoretical model," *Gondwana Res.* vol. 125, pp. 425–445, 2024.